Draft 5 (GRL= 5 pages max)

# Phase State and Physical Properties of Ambient and Laboratory Generated Secondary Organic Aerosol

**Rachel E. O'Brien,[1, 2*] Alexander Neu,[1] Scott A. Epstein,[3] Amanda C. MacMillan,[3] Sergey A. Nizkorodov,[3] Alexander Laskin,[4] Ryan C. Moffet,[2] Mary K. Gilles,[1]**

[1] Lawrence Berkeley National Laboratory, Berkeley, California, 94720-8198, USA

[2] Department of Chemistry, University of the Pacific, Stockton, CA 95211, USA

[3] Department of Chemistry, University of California, Irvine, CA 92697-2025, USA

[4] William R. Wiley Environmental and Molecular Sciences Laboratory, Pacific Northwest National Laboratory, Richland, WA, 99352, USA

*Address correspondence to the following author

Email: resellon@lbl.gov

Address: Lawrence Berkeley National Lab, 1 Cyclotron Road, mail stop 2R0300, Berkeley CA 94720-8198

Key Points:

Organic aerosol particle deformation is analyzed with x-ray microscopy

Amount of deformation is related to viscosity and surface tension of particles

Deformation of ambient and laboratory generated particles are compared

Index Terms

Atmospheric Composition and Structure: Aerosols and particles, instruments and techniques

Keywords

Aerosol, viscosity, STXM, microscopy

**Abstract**

The size and thickness of organic aerosol particles from five field campaigns were compared to those of laboratory generated secondary organic aerosols (SOA) using scanning transmission x-ray microscopy (STXM). Impacted organic particles were identified and the total carbon absorbance (TCA) was analyzed as a function of the area equivalent diameter of the particle on the substrate. Because they flatten less upon impaction, particles with higher viscosity and surface tension can be identified by a steeper slope on a plot of TCA vs. size. The slopes of the ambient data are statistically similar indicating a small range of average viscosities and surface tensions across five field campaigns. Steeper slopes were observed for the plots corresponding to ambient particles, while smaller slopes were indicative of the laboratory generated SOA. This suggests that, on average, ambient organic particles have higher viscosities and surface tensions than the more liquid like laboratory generated SOA particles.

## 1. Introduction

Organic aerosols constitute a significant fraction of atmospheric fine mode particulate matter [*Zhang et al.*, 2007]. Models of secondary organic aerosol (SOA) formation and aging assume that SOA consists of liquid particles with condensed phase diffusion rates that are fast enough to maintain equilibrium with the gas phase [*Pankow*, 1994; *Hallquist et al.*, 2009]. However, recent studies examining particle bounce behavior [*Virtanen et al.*, 2010], response to physical manipulation [*Renbaum-Wolff et al.*, 2013], evaporation [*Vaden et al.*, 2011; *Abramson et al.*, 2013; *Loza et al.*, 2013], thermal desorption [*Cappa and Wilson*, 2011], particulate nitrate uptake [*Perraud et al.*, 2012], ammonia uptake [*Kuwata and Martin*, 2012], and diffusion [*Vaden et al.*, 2010] provide evidence that both laboratory and ambient particles can have higher viscosities. Most studies have been done on small sample sizes with little inter-comparison across ambient samples and only few studies [*Virtanen et al.*, 2010; *Vaden et al.*, 2011] compared laboratory and ambient samples. An investigation of the phase state or viscosity of particles from different geographical locations and under a range of conditions would provide an opportunity to examine existing assumptions about chemical composition and kinetics and to constrain the range of viscosity values appropriate for SOA models.

When an aerosol particle impacts a surface, some kinetic energy is dissipated in deformation. If the kinetic energy loss is large enough that the adhesion energy exceeds the rebound energy, the particle will remain on the surface. The elastic properties (viscosity), the surface properties (surface tension), and the liquid flow properties (whether the material is non-Newtonian or not) [*Ivosevic et al.*, 2006] determine both the adhesion probability and the final shape of the impacted particle. In this work, we compare the size and thickness of the impacted particles measured by scanning transmission X-ray microscopy/near-edge X-ray absorption fine

72 structure (STXM/NEXAFS) in order to probe particle deformation and provide useful
73 information on particle properties.
74
75 **2. Experimental**
76 Ambient aerosols were collected over five field campaigns between 2001 and 2010.
77 Figure 1 shows the geographic locations of these field sites. All of the campaigns were in North
78 and South America. Two were in California: CARES (2010) in the Sacramento Valley [*Zaveri*
79 *et al.*, 2012] and YACS (2002) in Yosemite National Park [*Hand et al.*, 2005]. The NAOPEX
80 campaign (2001) [*Zaveri et al.*, 2010], MILAGRO campaign (2006) [*Moffet et al.*, 2010a], and
81 VOCALS (2008) [*Wood et al.*, 2011] took place in the Boston area, the Mexico City
82 metropolitan area, and in Chile respectively.
83 Laboratory samples were generated using a 5 $m^3$ Teflon chamber with UV-B broadband
84 lamps in the absence of inorganic seed particles [*Nguyen et al.*, 2011a]. All chamber
85 experiments were done in a dry chamber (relative humidity (RH) < 2%) that was flushed
86 overnight with dried air between experiments. The isoprene samples had ~100 μl $H_2O_2$ (Aldrich,
87 30% by volume in water) injected into a glass bulb and evaporated into the chamber with dry air
88 followed by a similar injection and evaporation of ~20 μl of isoprene (Aldrich, 99% purity). For
89 the high $NO_x$ ($HNO_x$) experiments, a small, controlled volume of gas from a NO cylinder
90 (Praxair, 5000 ppm NO in $N_2$) was injected in the chamber. The starting mixing ratios of
91 isoprene and $H_2O_2$ were 1 ppm and 6 ppm, respectively. For the $HNO_x$ experiment, the initial
92 mixing ratios of NO and $NO_y$ were ~400 and 500 ppb, respectively; the NOx level was below the
93 detection limit (2 ppb) in the low-NOx ($LNO_x$) experiments. Photooxidation times were 2-3
94 hours. Limonene SOA was generated by injecting *d*-limonene (10 μl → 300 ppb) and ozone

(~600 ppb) into the dry, dark chamber. Additional samples were prepared using a flow tube [*Bones et al.*, 2010]. Either *d*-limonene or α-pinene was introduced into a flow of zero air ($H_2O$, $CO_2$, and VOC's removed) and dry ozone using a syringe pump at liquid flow rates of 16 and 25 μl/hr, respectively. Additional information on particle generation and instrumentation is provided in the auxiliary material.

Ambient samples were collected using a TRAC (time-resolved aerosol collector) sampler with an effective cutoff size, $d_{50}$, of 0.36-0.38 μm [*Laskin et al.*, 2006]. Copper-grid-supported carbon B films and silicon nitride ($Si_3N_4$) coated Si frames were used as impaction substrates. Minimal differences in impaction behavior and, since both substrates are hydrophobic, minimal differences in the effect on surface tension are expected between the two substrates. Laboratory samples were collected on the seventh and eighth stages of a rotating MOUDI (multi-orifice uniform-deposit impactor, MSP 110-R) with aerodynamic cut points of 0.32 μm and 0.18 μm, respectively [*Marple et al.*, 1991] using $Si_3N_4$ coated Si frames as substrates. The impactor RH is equal to the ambient RH times the ratio of the impactor pressure to the ambient pressure [*Saukko et al.*, 2012]. Since the absolute pressure at the exit of the MOUDI's sixth and seventh stages is 95-97% of the inlet pressure, the particles experience negligible changes in RH during impaction. For the TRAC, the pressure in the sampling area is reduced to 70% of the ambient pressure, but, the ~30 μs spent in the impaction region (between the nozzle and the impaction surface) is insufficient for equilibration of the ~300-400 nm aerodynamic diameter particles with respect to the water uptake/loss prior to impaction [*Koop et al.*, 2011; *Saukko et al.*, 2012]. However, since the samples remain in the reduced pressure region, after impaction, for the duration of the sampling time, loss of higher volatility compounds is likely. The amount of loss may be sample dependent, and this is a potential source for some of the scatter in the data.

118 The final particle shape is related to the impaction velocity/kinetic energy, the viscosity
119 and surface tension, and the fluid flow properties [*Ivosevic et al.*, 2006]. In the TRAC sampler,
120 the particle impaction velocity is ~90 m/s, while in the MOUDI, on stage 7, the velocity is ~36
121 m/s [*Marple et al.*, 1991; *Laskin et al.*, 2006]. Therefore, any comparison between samples
122 collected with these two techniques must take into account that, due to the difference in
123 impaction velocities, identical particles collected with the TRAC will deform more than similar
124 particles collected with the MOUDI.
125 The scanning transmission X-ray microscopy/near-edge X-ray absorption fine structure
126 (STXM/NEXAFS) measurements were taken at the Advanced Light Source at Lawrence
127 Berkeley National Laboratory on beamlines 11.0.2 and 5.3.2.2. The operation of the microscope
128 has been explained in detail by Kilcoyne et al. [2003]. Briefly, samples were held at the focal
129 point (30-40 nm spot size) and raster scanned. Transmitted X-rays were detected, the X-ray
130 photon energy was incremented, and images at four energies (278, 285.4, 288, and 320 eV) were
131 collected. The work presented here uses analysis of images collected at the carbon K-edge,
132 focusing on 278 and 320 eV. These energies correspond to absorbance due to the carbon pre-
133 edge and post-edge, respectively [*Moffet et al.*, 2010b]. The STXM measurements were
134 performed under vacuum; an initial pump down to ~100 mTorr and then backfilled with He to 20
135 Torr.
136 STXM/NEXAFS data were imported into MatLab software for further analysis [*Moffet et*
137 *al.*, 2010b]. The pixels determined to contain particles were assigned an intensity value ($I$), the
138 particle-free pixels were assigned a background intensity value ($I_0$), and the absorbance or optical
139 density (OD) was calculated via the equation:
140

$$OD = -\ln(I/I_0) = \mu\rho d \quad \text{Equation 1}$$

where $\mu$ is the mass absorption coefficient ($cm^2/g$), $\rho$ is the density ($g/cm^3$), and $d$ is the thickness of the particle (cm). By examining the difference in optical density between the post-edge and the pre-edge, the thickness of the carbon or the total carbon absorbance (TCA) can be calculated (subscripts correspond to the X-ray photon energies) [*Moffet et al.*, 2011].

$$TCA = OD_{320} - OD_{278} \quad \text{Equation 2}$$

Three component types were identified by the MatLab script: organic, inorganic, and elemental carbon or soot [*Moffet et al.*, 2010b]. Only particles identified as predominantly organic, without any inorganic dominant regions or soot inclusions, were selected for the data sets presented in this manuscript. Some particles and particle components were non-spherical; hence, the sizes are reported as area equivalent diameters (AED). The auxiliary material contains additional information on the data collection and analysis.

## 3. Results and Discussion

Figure 2 displays the best fit lines for the size of impacted particles vs. the TCA for all data sets. The data for the ambient particles are shown with solid lines and dashed lines are used for the laboratory particles. A steeper slope indicates that the particles have flattened less during impaction, and thus, have a higher viscosity and/or surface tension. Plots of full data sets and corresponding fitting parameters are provided in Figures S1-S2 and Tables S1-S2. The red and blue shaded areas highlight the range of the ±95% confidence intervals for the ambient and

laboratory particles respectively. The slope of each ambient data set falls within the 95% confidence intervals of the other data sets consistent with similar viscosities and/or surface tensions between the samples. This similarity indicates that a small range of viscosity and/or surface tension values may adequately describe the average aerosol population used in SOA models.

In Figure 2 all of the laboratory samples have smaller slopes than ambient samples. Four of the laboratory samples' slopes lie within the 95% confidence intervals of the each other. Thus, the different oxidants, precursors, and different conditions (chamber vs. flow tube) sampled here have minimal effect on the viscosities and/or surface tensions of the aerosols formed. The isoprene sample generated under $HNO_x$ conditions is the outlier, outside the 95% confidence intervals of the other samples, with a slightly negative slope. The negative slope arises because the slope of $OD_{320}$ vs. size (Table S3) is nearly zero and the $OD_{278}$ is slightly higher, but within the 95% confidence interval, than the $OD_{320}$. Pre-edge absorbance ($OD_{278}$) arises from absorption and a small contribution from scattering of other atoms such as nitrogen, oxygen, sulfur, etc. Post-edge absorbance ($OD_{320}$) is due to absorption and scattering from carbon as well as the other atoms. Photooxidation of isoprene under $HNO_x$ conditions is known to generate compounds with higher O/C ratio and significant nitrogen content compared to the $LNO_x$ conditions [*Nguyen et al.*, 2011b]. However, since the slope of the $OD_{320}$ vs. size is outside the 95% confidence intervals of the other laboratory samples (Table S3) the scattering and absorption by the heteroatoms does fully account for the smaller slope for the $HNO_x$ sample, which means the particles have a lower viscosity/surface tension. Potential reasons for these differences include (1) isoprene particles formed under $HNO_x$ conditions and under $LNO_x$ conditions have different chemical compositions [*Nguyen et al.*, 2011b] and (2) the $HNO_x$

aerosols formed more quickly and were in the chamber for a shorter period of time (~2 hrs. for $HNO_x$ vs. ~3 hrs. for the $LNO_x$ experiments).

The difference between ambient and laboratory aerosol particles is consistent with observations of slower evaporation kinetics for ambient SOA compared to laboratory generated SOA [*Vaden et al.*, 2011]. However, Virtanen et al. [2010] reported a higher bounce fraction for chamber SOA than that for atmospheric SOA which is consistent with higher viscosity/more glassy particles in their chamber compared to the ambient. It is important to note that their chamber SOA was generated from a mixture of all of the volatile organic compounds (VOCs) emitted by pine seedlings. Thus, a difference between our results and the results of Virtanen could be that our laboratory experiments used a single VOC precursor rather than a complex mixture.

A variety of techniques have indicated that laboratory generated particles are amorphous semi-solid particles [*Vaden et al.*, 2010; *Virtanen et al.*, 2010; *Cappa and Wilson*, 2011; *Vaden et al.*, 2011; *Kuwata and Martin*, 2012; *Perraud et al.*, 2012]. In contrast, the data from this study show that the laboratory generated particles have smaller slopes than the ambient particles. The analysis presented here examines deformation behavior of particles upon impaction. Since deformation depends upon both viscosity and surface tension, a direct comparison between the relative deformation behaviors observed here and the viscosities reported in other studies should be made with caution. However, the laboratory conditions used here are fairly typical, and thus, the results showing lower viscosity/surface tension for laboratory particles compared to ambient particles are relevant for a wide range of laboratory studies.

Figure 3 shows the particle size as a function of the optical density at the pre-edge, $OD_{278}$. The black data points are the combined ambient data and the red data points are the

combined laboratory generated data. The slope of the best fit line for the ambient data is an order of magnitude higher than the slope for the laboratory generated particles. The pre-edge absorbance is due to absorbance and scattering by atoms other than carbon such as O, N, S, etc. and the difference in slopes indicate that the ambient particles have more heteroatoms than the laboratory generated particles. Most likely, there are significantly more organo-sulfates and organo-nitrates in the ambient particles, or there are small amounts of inorganic species such as $(NH_4)_2SO_4$, that do not crystalize into a large inclusion and are instead finely dispersed through the particle. The contribution from other absorbing and scattering elements was estimated by calculating the thickness ratio of organic to inorganic components using $OD_{278}$ and $OD_{320}$ measurements and estimates of the mass absorption coefficients and densities for both organic and inorganic species (for calculations see Auxiliary material). Approximately 11-30% of the thickness for the particles is likely due to non-organic molecules or atoms. The most likely species are $(NH_4)_2SO_4$ and NaCl, but nano-particles that contain other elements commonly observed in atmospheric aerosols [*Moffet et al.*, 2010a] are also possible.

There are numerous possible reasons for the observed differences between laboratory generated and ambient aerosols. Aerosols in smog chambers are more concentrated prompting smaller, semi-volatile organic compounds (SVOC), which would normally exist in gaseous phase under typical ambient conditions, to partition in particles, potentially making the particles more liquid like. The semi-volatile compounds may be lost during measurements since STXM is performed under vacuum and the potentially larger amount of SVOC in the chamber experiments could make the particles more optically thin. Chamber particles have reacted for a shorter length of time than aerosols in the ambient environment [*Ng et al.*, 2010]. In the chamber experiments only a single precursor was used, whereas ambient samples can have a wide range of precursors.

Finally, no inorganic compounds were used in the chamber studies which may impact the chemical composition of the particles and ultimately the particle phase state. Our results demonstrate that the chemical compositions and potentially the reaction kinetics of laboratory aerosols differ significantly from those in the ambient environment.

## 4. Summary and Conclusions

We investigated the amount of deformation of impacted aerosol particles from both ambient field campaigns and laboratory studies using STXM/NEXAFS analysis of the TCA and the size of the particles. Samples with steeper slopes on a plot of TCA vs. size have higher viscosities/surface tensions. The slopes for the ambient samples all fell within the 95% confidence interval of each other. The laboratory generated samples all had lower slopes than the ambient samples indicating lower viscosities/surface tensions than for particles measured during ambient field campaigns. The differences in aging time, aerosol mass concentration, volatility, number of precursors, and lack of any inorganic compounds in the laboratory samples likely contribute to these results. The lower viscosities/surface tensions in the laboratory samples impacts the kinetics of SOA formation, gas-particle partitioning, and chemical composition of the laboratory generated aerosols as compared to ambient aerosols. Thus, caution should be used when comparing the results of laboratory experiments to ambient samples and when applying data from laboratory studies to SOA models. The results of this study indicate that a small range of viscosities/surface tensions may be appropriate to describe the average ambient aerosol population in SOA models.

## Acknowledgements

Data supporting Figure 2 and Figure 3 are available in the Supporting information, Table S6.

This work was supported in part by the U.S. Department of Energy's Atmospheric System Research, an Office of Science, Office of Biological and Environmental Research program. STXM/NEXAFS was done at beamlines 5.3.2.2 and 11.0.2 at The Advanced Light Source at Lawrence Berkeley National Laboratory (LBNL).which are supported by the Director, Office of Science, Office of Basic Energy Sciences, (beamline 11.0.2 is also supported by the Division of Chemical Sciences, Geosciences, and Biosciences) of the U.S. Department of Energy under Contract No. DE-AC02-05CH11231. The UCI team acknowledges support from the National Science Foundation Grant CHE-0909227.

1.

285

286

287

288

289

290

291

292

293

294

295

296

297

298

299 **References**

300 Abramson, E., et al. (2013), Experimental determination of chemical diffusion within secondary
301 organic aerosol particles, *Physical Chemistry Chemical Physics 15*(8): 2983-2991.
302 Bones, D. L., et al. (2010), Appearance of strong absorbers and fluorophores in limonene-$O_3$
303 secondary organic aerosol due to $NH_4^+$-mediated chemical aging over long time scales,
304 *Journal of Geophysical Research-Atmospheres, 115*, D05203, doi:10.1029/2009JD012864.
305 Cappa, C. D. and K. R. Wilson (2011), Evolution of organic aerosol mass spectra upon heating:
306 implications for OA phase and partitioning behavior, *Atmospheric Chemistry and Physics*
307 *11*(5): 1895-1911.
308 Hallquist, M., et al. (2009), The formation, properties and impact of secondary organic aerosol:
309 current and emerging issues, *Atmospheric Chemistry and Physics 9*(14): 5155-5236.

Hand, J. L., et al. (2005), Optical, physical, and chemical properties of tar balls observed during the Yosemite Aerosol Characterization Study. *Journal of Geophysical Research-Atmospheres 110*, D21210, doi:10.1029/2004JD005728.

Ivosevic, M., et al. (2006), 3D predictions of thermally sprayed polymer splats: Modeling particle acceleration, heating and deformation on impact with a flat substrate, *International Journal of Heat and Mass Transfer 49*(19-20): 3285-3297.

Kilcoyne, A. L. D., et al. (2003), Interferometer-controlled scanning transmission X-ray microscopes at the Advanced Light Source, *Journal of Synchrotron Radiation 10*: 125-136.

Koop, T., et al. (2011), Glass transition and phase state of organic compounds: dependency on molecular properties and implications for secondary organic aerosols in the atmosphere, *Physical Chemistry Chemical Physics 13*(43): 19238-19255.

Kuwata, M. and S. T. Martin (2012), Phase of atmospheric secondary organic material affects its Reactivit, *Proceedings of the National Academy of Sciences of the United States of America 109*(43): 17354-17359.

Laskin, A., et al. (2006), Analysis of individual environmental particles using modern methods of electron microscopy and X-ray microanalysis, *J. Electron Spectrosc. Relat. Phenom. 150*(2-3): 260-274.

Loza, C. L., et al. (2013), On the Mixing and Evaporation of Secondary Organic Aerosol Components, *Environmental Science & Technology 47*(12): 6173-6180.

Marple, V. A., et al. (1991), A Microorfice Uniform Deposit Impactor (MOUDI) - Description, Calibration, And Use*, Aerosol Science and Technology 14*(4): 434-446.

Moffet, R. C., et al. (2010a), Microscopic characterization of carbonaceous aerosol particle aging in the outflow from Mexico City, *Atmospheric Chemistry and Physics 10*(3): 961-976.

Moffet, R. C., et al. (2010b), Automated Chemical Analysis of Internally Mixed Aerosol Particles Using X-ray Spectromicroscopy at the Carbon K-Edge, *Anal Chem 82*(19): 7906-7914.

Moffet, R. C., et al. (2011). Scanning Transmission X-ray Microscopy Applications in Atmospheric Aerosol Research, Fundamentals and Applications in Aerosol Spectroscopy. R. Signorell and J. P. Reid. Boca Raton, Fl, CRC Press, Taylor & Francis Group**:** 434-436.

Ng, N. L., et al. (2010), Organic aerosol components observed in Northern Hemispheric datasets from Aerosol Mass Spectrometry, *Atmospheric Chemistry and Physics 10*(10): 4625-4641.

Nguyen, T. B., et al. (2011a), Effect of humidity on the composition of isoprene photooxidation secondary organic aerosol, *Atmospheric Chemistry and Physics 11*(14): 6931-6944.

Nguyen, T. B., et al. (2011b), Nitrogen-Containing Organic Compounds and Oligomers in Secondary Organic Aerosol Formed by Photooxidation of Isoprene, *Environmental Science & Technology 45*(16): 6908-6918.

Pankow, J. F. (1994), An Absorption-Model of Gas-Particle Partitioning of Organic-Compounds In The Atmosphere, *Atmospheric Environment 28*(2): 185-188.

Perraud, V., et al. (2012), Nonequilibrium atmospheric secondary organic aerosol formation and Growth, *Proceedings of the National Academy of Sciences of the United States of America 109*(8): 2836-2841.

Renbaum-Wolff, L., et al. (2013), Viscosity of alpha-pinene secondary organic material and implications for particle growth and reactivity*, Proceedings of the National Academy of Sciences of the United States of America 110*(20): 8014-8019.

Saukko, E., et al. (2012), A method to resolve the phase state of aerosol particles, *Atmospheric*

*Measurement Techniques 5*(1): 259-265.
Vaden, T. D., et al. (2010), Morphology of mixed primary and secondary organic particles and the adsorption of spectator organic gases during aerosol formation*, Proceedings of the National Academy of Sciences of the United States of America 107*(15): 6658-6663.
Vaden, T. D., et al. (2011), Evaporation kinetics and phase of laboratory and ambient secondary organic aerosol*, Proceedings of the National Academy of Sciences of the United States of America 108*(6): 2190-2195.
Virtanen, A., et al. (2010), An amorphous solid state of biogenic secondary organic aerosol Particles, *Nature 467*(7317): 824-827.
Wood, R., et al. (2011), The VAMOS Ocean-Cloud-Atmosphere-Land Study Regional Experiment (VOCALS-REx): goals, platforms, and field operations*, Atmospheric Chemistry and Physics 11*(2): 627-654.
Zaveri, R. A., et al. (2010), Nighttime chemical evolution of aerosol and trace gases in a power plant plume: Implications for secondary organic nitrate and organosulfate aerosol formation, $NO_3$ radical chemistry, and $N_2O_5$ heterogeneous hydrolysis, *Journal of Geophysical Research-Atmospheres 115*, D12304, doi:10.1029/2009JD013250.
Zaveri, R. A., et al. (2012), Overview of the 2010 Carbonaceous Aerosols and Radiative Effects Study (CARES), *Atmospheric Chemistry and Physics 12*(16): 7647-7687.
Zhang, Q., et al. (2007), Ubiquity and dominance of oxygenated species in organic aerosols in anthropogenically-influenced Northern Hemisphere midlatitudes*, Geophysical Research Letters 34*(13), L13801, doi:10.1029/2007GL029979.

**Table 1**. Ambient and laboratory fitting results for TCA vs. size[a]

| Campaign | Slope | Intercept | Sample | Slope | Intercept |
|---|---|---|---|---|---|
| CARES | 0.090±0.004 | 0.0079±0.002 | Isoprene-LNOx | 0.031±0.006 | 0.025±0.003 |
| MILAGRO | 0.077±0.01 | 0.029±0.005 | Isoprene-HNOx | -0.011±0.01 | 0.023±0.005 |
| NAOPEX | 0.084±0.01 | 0.020±0.01 | α-pinene-flow tube | 0.036±0.008 | 0.048±0.009 |

| | | | | | |
|---|---|---|---|---|---|
| VOCALS | 0.10±0.03 | 0.018±0.01 | Limonene-flow tube | 0.039±0.009 | 0.023±0.005 |
| YACS | 0.11±0.03 | 0.0043±0.01 | Limonene-chamber | 0.042±0.006 | 0.028±0.005 |

[a]The ±95% confidence intervals for the slope and intercept are given.

## Figures


403

404 **Figure 1.** Map showing the geographic locations of the five field campaigns. Samples from the
405 VOCALS campaign in Chile and the NAOPEX campaign in the Boston area were aerial
406 samples, MIAGRO, CARES, and YACS samples were collected at the ground sites.

407

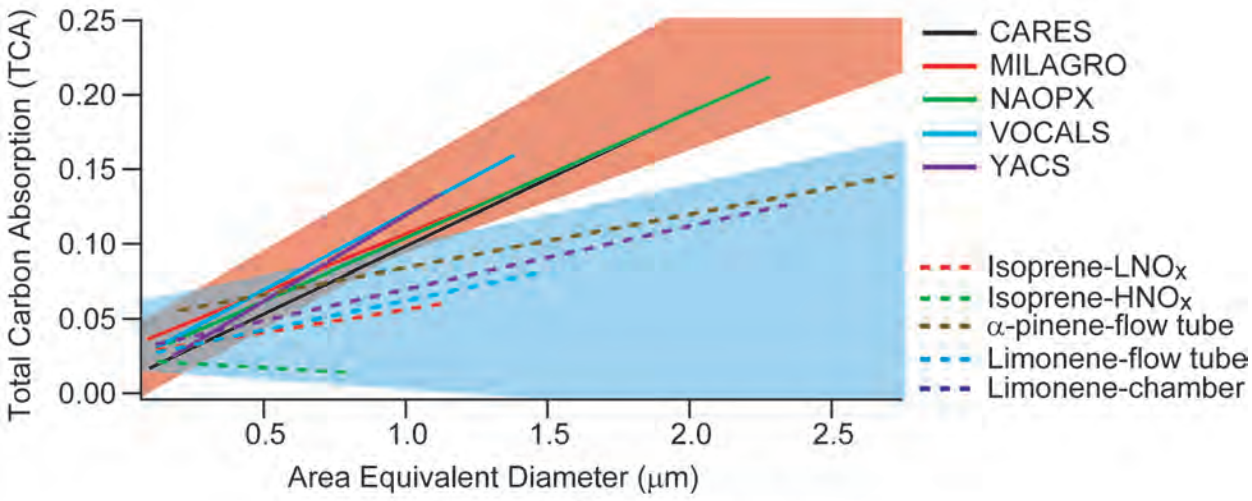


408
409 **Figure 2.** Optical thickness of carbon (total carbon absorption) as a function of size of the

impacted organic particles. Solid lines: best fit lines for the ambient particles, dashed lines: best fit lines for the laboratory generated particles. The red and blue triangles highlight the range of the ±95% confidence intervals for the ambient and laboratory samples respectively. $LNO_x$ and $HNO_x$ refer to low-$NO_x$ and high-$NO_x$ oxidation by OH; ozone is used as the oxidant for the remaining samples.

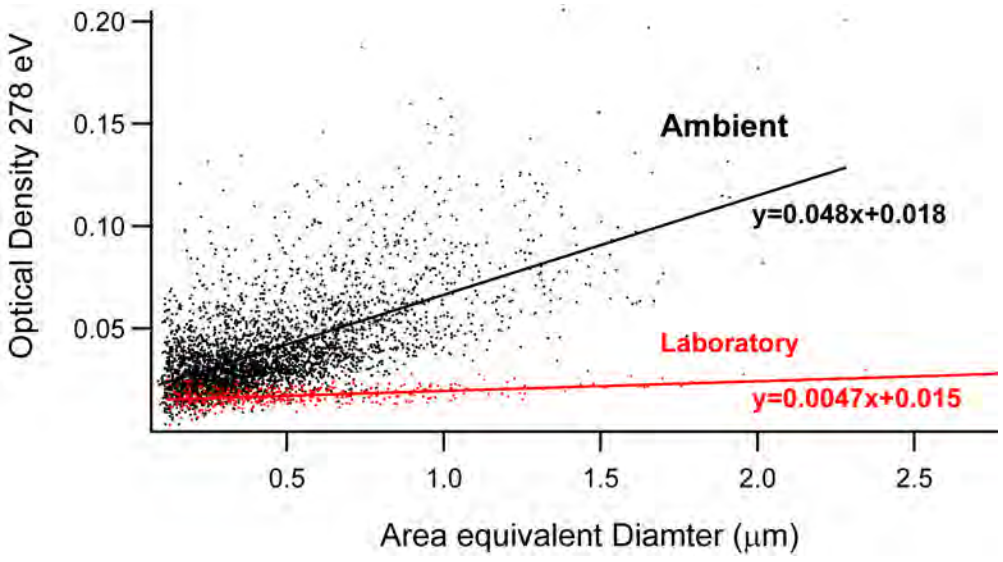

425 **Figure 3.** Optical density at 278 eV (pre-edge) vs. size (area equivalent diameter). Black: all
426 ambient samples, red: all laboratory samples. The best fit lines and equations are shown for each
427 data set. The data are consistent with a higher fraction of non-carbon elements in the ambient
428 samples.

Draft 5

# Phase State and Physical Properties of Ambient and Laboratory Generated Secondary Organic Aerosol

**Rachel E. O'Brien,[1, 2*] Alexander Neu,[1] Scott A. Epstein,[3] Amanda C. MacMillan,[3] Sergey A. Nizkorodov,[3] Alexander Laskin,[4] Ryan C. Moffet,[2] Mary K. Gilles,[1]**

[1] Chemical Sciences Division, Lawrence Berkeley National Laboratory, Berkeley, California, 94720-8198, USA

[2] Department of Chemistry, University of the Pacific, Stockton, CA 95211, USA

[3] Department of Chemistry, University of California, Irvine, CA 92697-2025, USA

[4] William R. Wiley Environmental and Molecular Sciences Laboratory, Pacific Northwest National Laboratory, Richland, WA, 99352, USA

*Address correspondence to the following author

Email: resellon@lbl.gov

# Supplemental Information

## Laboratory generated samples

Experimental conditions for chamber experiments are given in Table S4 (the tables and figures are numbered in the order of appearance in the main manuscript). For the flow tube experiments, the flow tube was operated at low RH (< 2%), ambient temperature (~25 °C), with the lights turned off. The oxidant was ozone (30-50 ppm) produced by flowing oxygen gas through a commercial ozone generator. The flow tube residence time was ~5 min. In both cases (chamber and flow tube) samples were collected on stages 7 and 8 of a 10 stage rotating cascade impactor (MOUDI 110-R, MSP) using $Si_3N_4$ windows taped to aluminum substratestCollection times were ~30-45 min for chamber experiments and ~1 min for flow tube experiments.

## Data Collection/Analysis

Because of the poor signal to noise ratio, particles with average $OD_{320}$ values < 0.03 were excluded from analysis. For $I_o$ values of ~ 7,000 counts/ms, this cutoff corresponds to about 200 photons/ms. Since stray light in the STXM leads to approximately 100-200 photons/ms noise, the particles with the lowest average OD have the largest relative amount of noise.

Since some particles and particle components were non-spherical, the sizes reported are the area equivalent diameters (AED), defined as a diameter of a hemisphere required to cover the same area as the projection of the particles on the surface:

$$\mathrm{AED} = 2\sqrt{\left(\frac{length_x \times length_y}{\pi}\right)} \qquad \text{Equation S1}$$

where $length_x$ and $length_y$ are the effective sizes of the particle in the x and y dimensions.

**Absorption Coefficients**

Organic material mass absorption coefficients μ ($cm^2/g$) were obtained from the sum of the absorption cross sections of the constituent atoms by:

$$\mu = \frac{N_A}{MW} \sum_i x_i \sigma_{ai} \qquad \text{Equation S2}$$

where $MW$ is the molecular weight of the compound containing $x_i$ atoms of type $i$, $\sigma_a$ is the total atomic absorption cross section ($cm^2$/atom) for this type of atom, and $N_A$ is the Avogadro's number. This approximation neglects interactions between the atoms in the material and is applicable at photon energies sufficiently far from absorption edges [*Henke et al.*, 1993; *Thomson et al.*, 2009]. Using the list of chemical formulas from negative mode high resolution mass spectrometry analysis of ambient particles (O'Brien et al., manuscript in preparation, 2014), the mass absorption coefficient was calculated and plotted as a function of the O/C value (Figure S3). An estimate for the average O/C value of 0.44 [*Setyan et al.*, 2012] leads to $\mu_{320} \cong$ 22,500 $cm^2/g$ and $\mu_{278} \cong$ 1102 $cm^2/g$.

**Inorganic Contributions**

The particles used in this analysis were identified as organic using the MatLab script [*Moffet et al.*, 2010b]. However, aerosol particles that are primarily organic can also have inorganic components. To estimate the fraction of other elements in these particles we examined

the OD at the carbon pre-edge (278 eV) and the post edge (320 eV) of a particle with inorganic and organic components via equations S3 and S4:

$$OD_{278} = \mu_{org,278}\rho_{org}d_{org} + \mu_{in,278}\rho_{in}d_{in} \quad \text{Equation S3}$$

$$OD_{320} = \mu_{org,320}\rho_{org}d_{org} + \mu_{in,320}\rho_{in}d_{in} \quad \text{Equation S4}$$

Where $\mu_{org,}\rho_{org}$ is the linear absorption coefficient of the organic species, $\mu_{in,}\rho_{in}$ is the linear absorption coefficient for the inorganic species, and $d_{in}$ and $d_{org}$ are the average sample thicknesses of the inorganic and organic, respectively. The thickness ratio [*Moffet et al.*, 2010b] can then be calculated by combining equations S3 and S4:

$$\frac{d_{org}}{d_{in}} = \frac{OD_{320}\mu_{in,278}\rho_{in} - OD_{278}\mu_{in,320}\rho_{in}}{OD_{278}\mu_{org,320}\rho_{org} - OD_{320}\mu_{org,278}\rho_{org}} \quad \text{Equation S5}$$

To calculate the linear absorption coefficients for the organic terms, the $\mu_{320}$ and $\mu_{278}$ estimates from above and a density of 1.3 g/cm$^3$ [*Setyan et al.*, 2012] were used. For the inorganic terms, three cases were considered. In the first case, the linear absorption coefficients were calculated for elements with atomic numbers between 6 (carbon) and 26 (Iron) that have been observed in atmospheric aerosols [*Moffet et al.*, 2010a]. Elements with higher linear absorption coefficients will absorb more photons and at 278 eV Al, Si, P, S, Cr, Mg, and Fe all have higher linear absorption coefficients in the range of 7-13 μm$^{-1}$ (Figure S4a). At 320 eV the elements Si, P, S, Cl, Cr, Mn, and Fe all have coefficients between 5.6-10 μm$^{-1}$ (Figure S4b). Given these ranges, values of 10 μm$^{-1}$ at 278 eV and 8 μm$^{-1}$ at 320 eV were used. In the second case, the linear absorption coefficients for NaCl were used (8.1 μm$^{-1}$ at 278 eV and 6.3μm$^{-1}$ at 320 eV). In the

last case, values for ammonium sulfate were used (3.2 $\mu m^{-1}$ at 278 eV and 2.4 $\mu m^{-1}$ at 320 eV). Using these estimates and the measured $OD_{278}$ and $OD_{320}$ values, the average thickness ratio for each data set was calculated and is shown in Table S6. All of the data sets, with the exception of VOCALS, range from ~11-30% inorganic with higher percentages when all of the inorganic is assumed to be ammonium sulfate as the inorganic. The VOCALS data set has averages from ~22-47% indicating that the organic dominated particles in this campaign contain a larger contribution of inorganic species than the other campaigns. The particles from the VOCALS campaign were collected downwind of copper smelting plants with large sulfur emissions [*Wood et al.*, 2011]. Thus, for these campaigns, approximately 11-30% of the thickness for the organic particles is likely due to the absorption cross section contribution from non-organic molecules or atoms.

**References**


Henke, B. L., et al. (1993), X-Ray Interactions - Photoabsorption, Scattering, Transmission And Reflection at E=50-30,000 EV, Z=1-92 (VOL 54, PG 181, 1993). *Atom. Data Nucl. Data Tables 55*(2): 349-349.

Moffet, R. C., et al. (2010a), Microscopic characterization of carbonaceous aerosol particle aging in the outflow from Mexico City, *Atmospheric Chemistry and Physics 10*(3): 961-976.

Moffet, R. C., et al. (2010b), Automated Chemical Analysis of Internally Mixed Aerosol Particles Using X-ray Spectromicroscopy at the Carbon K-Edge, *Anal Chem 82*(19): 7906-7914.

Setyan, A., et al. (2012), Characterization of submicron particles influenced by mixed biogenic and anthropogenic emissions using high-resolution aerosol mass spectrometry: results from CARES, *Atmospheric Chemistry and Physics 12*(17): 8131-8156.

Thomson, A., et al. (2009). *Center for X-Ray Optics and Advanced Light Source X-Ray Data Booklet*. Lawrence Berkeley National Laboratory, Lawrence Berkeley National Laboratory.

Wood, R., et al. (2011), The VAMOS Ocean-Cloud-Atmosphere-Land Study Regional Experiment (VOCALS-REx): goals, platforms, and field operations, *Atmospheric Chemistry and Physics 11*(2): 627-654.

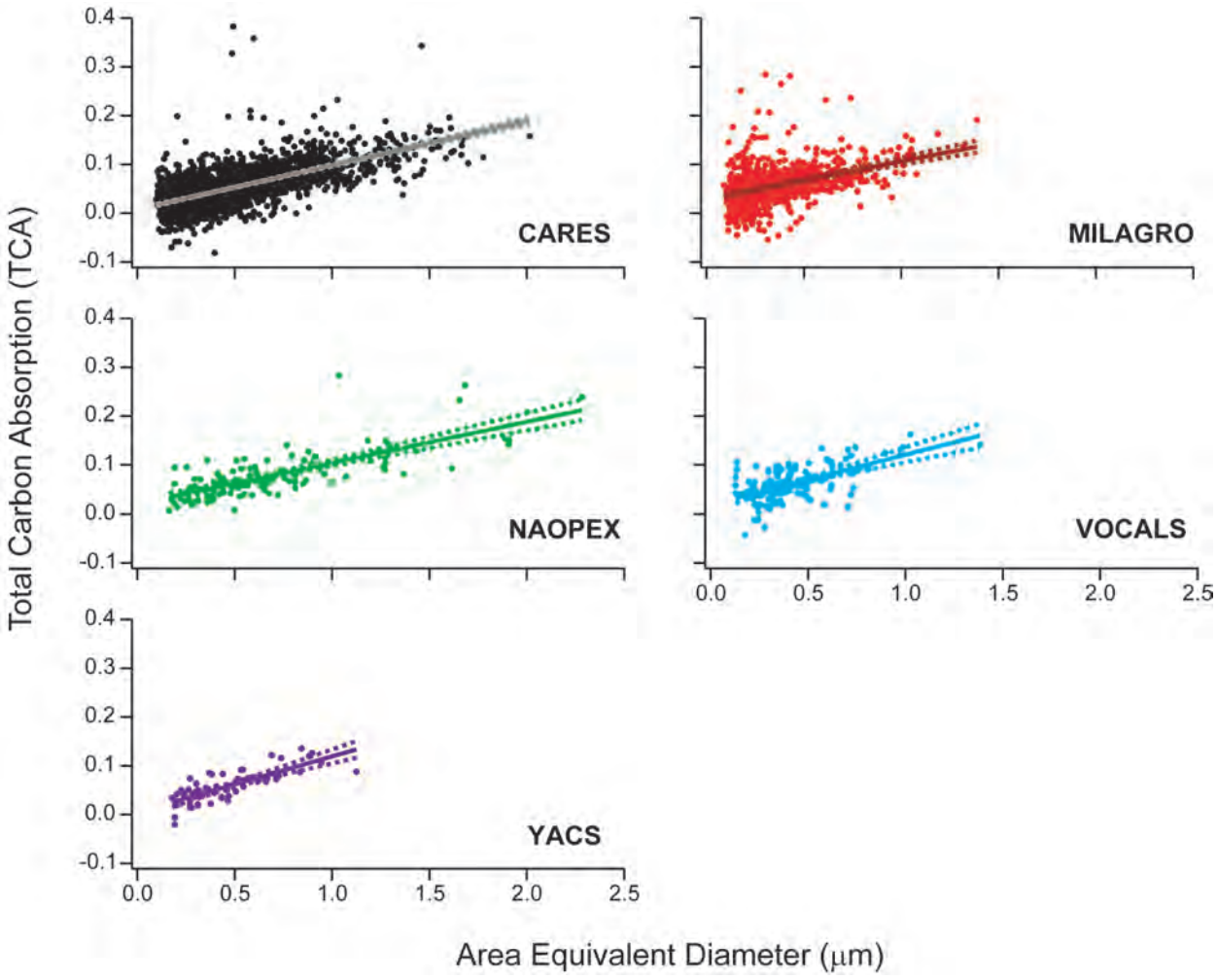


**Figure S1.** Optical thickness of carbon (total carbon absorption = $OD_{320}$-$OD_{278}$) as a function of size of impacted organic particles for each ambient data set. Solid lines are best fit lines for each data set and dashed lines are ±95% confidence intervals. The thick fitted lines are reproduced in Figure 2 of the main text, and the slopes, intercepts, and confidence intervals are listed in Table 1.

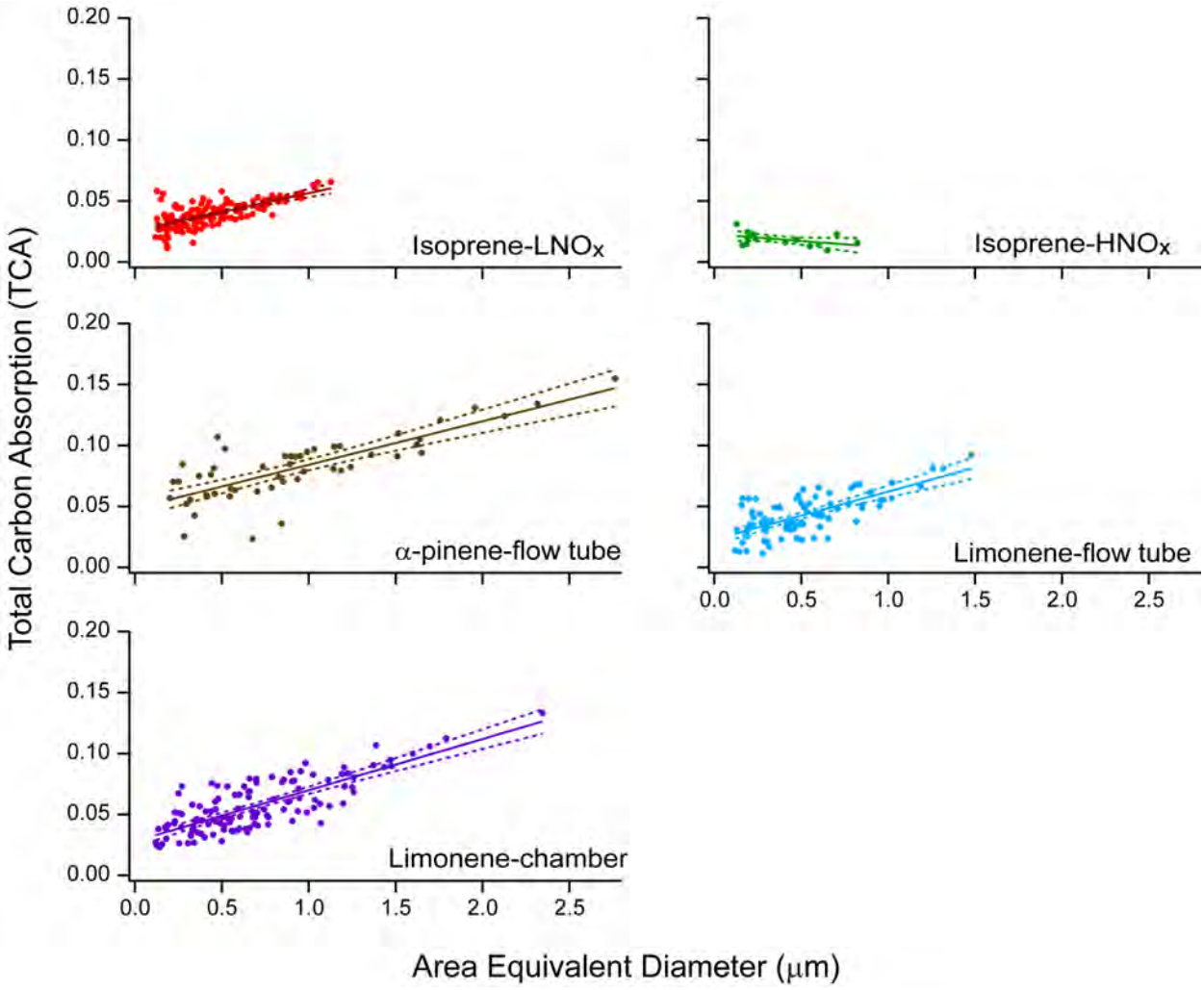


**Figure S2.** Optical thickness of carbon (total carbon absorption = $OD_{320}$-$OD_{278}$) as a function of size of impacted organic particles for each laboratory data set. Solid lines are best fit lines for each data set; the same lines are reproduced in Figure 2 of the main text. The slopes are listed in Table 1.

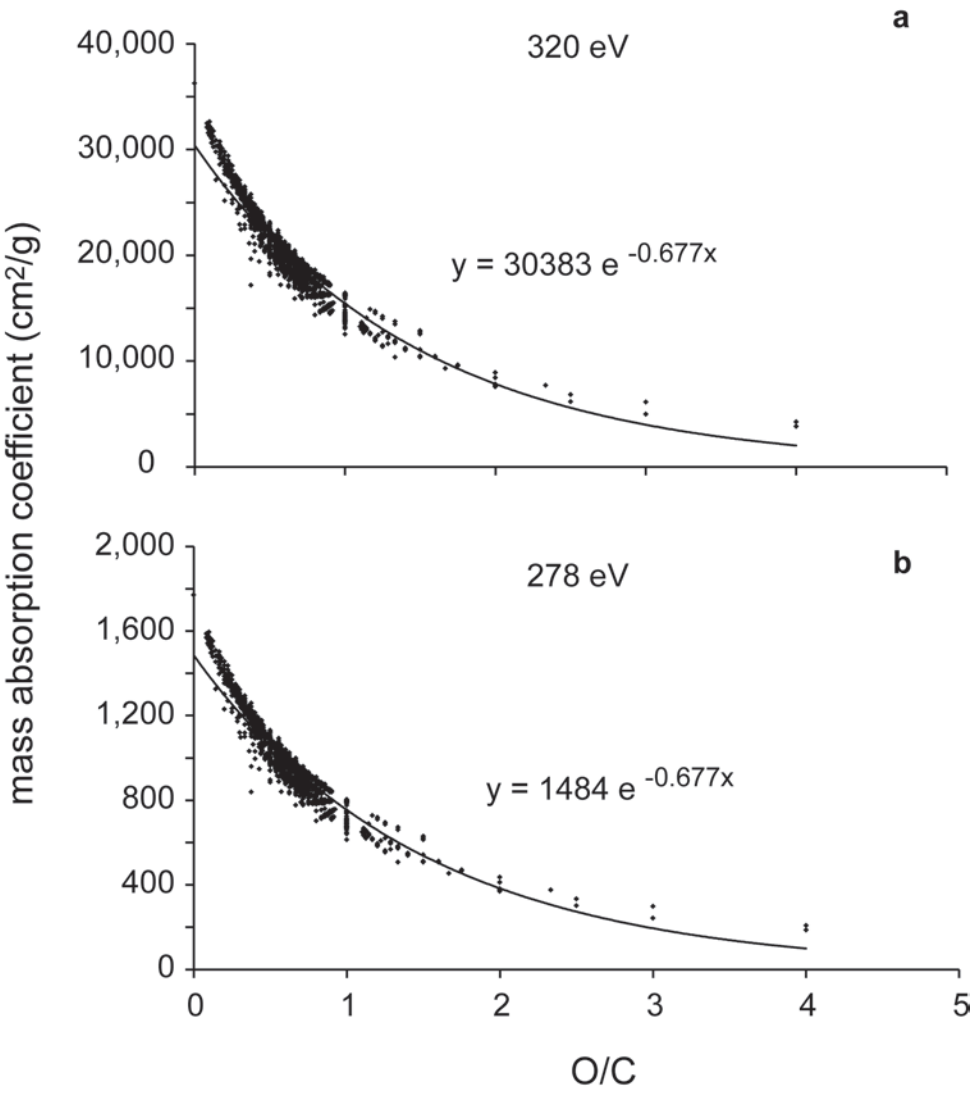


**Figure S3.** Calculated mass absorption coefficients as a function of O/C at a) 320 eV and b) 278 eV for chemical formulas from organic molecules found in atmospheric aerosols.

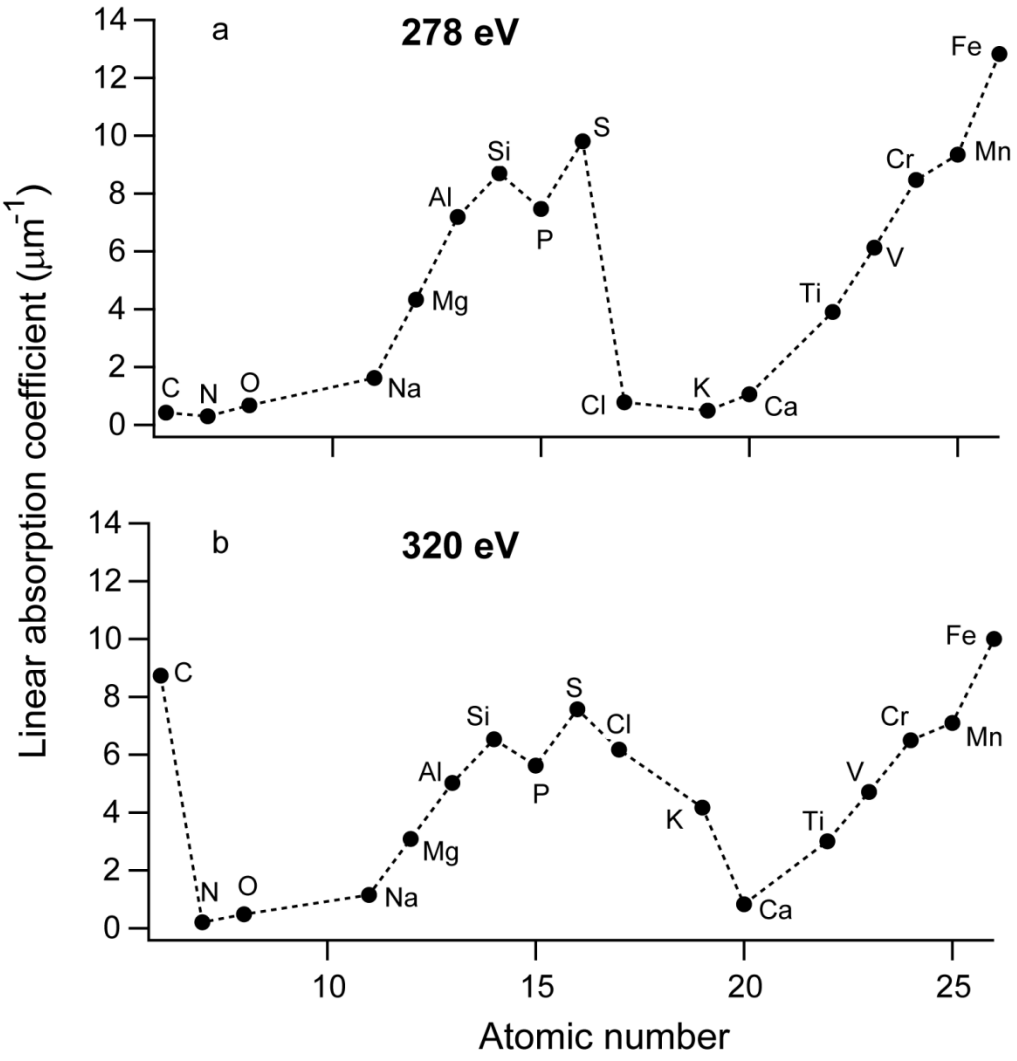


**Figure S4.** Linear absorption coefficients at (a) 278 eV and (b) 320 eV for elements found in atmospheric aerosols [*Henke et al.*, 1993].

**Table S1.** Ambient sample collection information and fitting results for $OD_{320}$ and $OD_{278}$ vs. area equivalent diameter.[a]

| | | | 320 eV | | 278 eV | |
|---|---|---|---|---|---|---|
| **Campaign** | **Year** | **Number of particles** | **Slope** | **Intercept** | **Slope** | **Intercept** |
| CARES | 2010 | 2428 | 0.14±0.005 | 0.024±0.003 | 0.045±0.002 | 0.016±0.001 |
| MILAGRO | 2006 | 798 | 0.13±0.01 | 0.048±0.005 | 0.057±0.005 | 0.019±0.002 |
| NAOPEX | 2001 | 123 | 0.15±0.02 | 0.028±0.01 | 0.069±0.007 | 0.008±0.006 |
| VOCALS | 2008 | 125 | 0.20±0.04 | 0.042±0.02 | 0.098±0.02 | 0.023±0.01 |
| YACS | 2002 | 56 | 0.14±0.02 | 0.029±0.01 | 0.027±0.01 | 0.025±0.006 |

[a]The ±95% confidence intervals for the slope and intercept are given.

**Table S2.** Laboratory sample fitting results for total carbon absorption (TCA) vs. area equivalent diameter.[a]

| Sample | MOUDI stage | Number of particles | Slope | Intercept | $R^2$ |
|---|---|---|---|---|---|
| Isoprene-LNOx | 7 | 137 | 0.031±0.006 | 0.025±0.003 | 0.48 |
| Isoprene-HNOx | 7 | 16 | -0.011±0.01 | 0.023±0.005 | 0.22 |
| α-pinene-flow tube | 7 | 51 | 0.036±0.008 | 0.048±0.009 | 0.63 |
| Limonene-flow tube | 7 | 87 | 0.039±0.009 | 0.023±0.005 | 0.49 |
| Limonene-chamber | 8 | 122 | 0.042±0.006 | 0.028±0.005 | 0.62 |

[a]The ±95% confidence intervals for the slope and intercept are given. LNOx and HNOx refer to low-NOx and high-NOx oxidation by OH; ozone is used as the oxidant for the remaining samples.

**Table S3.** Laboratory sample fitting results for $OD_{320}$ and $OD_{287}$ vs. area equivalent diameter.[a]

| | 320 eV | | 278 eV | |
|---|---|---|---|---|
| **Sample** | **Slope** | **Intercept** | **Slope** | **Intercept** |
| Isoprene-$LNO_x$ | 0.039±0.004 | 0.040±0.002 | 0.0083±0.002 | 0.014±0.001 |
| Isoprene-$HNO_x$ | 0.0036±0.009 | 0.033±0.004 | 0.015±0.007 | 0.011±0.003 |
| α-pinene-flow tube | 0.040±0.008 | 0.063±0.009 | 0.0042±0.001 | 0.015±0.001 |
| Limonene-flow tube | 0.042±0.008 | 0.037±0.005 | 0.0027±0.002 | 0.014±0.001 |
| Limonene-chamber | 0.047±0.006 | 0.043±0.005 | 0.0049±0.002 | 0.015±0.001 |

[a]The ±95% confidence intervals for the slope and intercept are given. $LNO_x$ and $HNO_x$ refer to low-$NO_x$ and high-$NO_x$ oxidation by OH; ozone is used as the oxidant for the remaining samples.

**Table S4.** Summary of experimental conditions for the chamber experiments[a]

| Sample | [HC] ppm | Oxidant precursor | [NO] ppb | [$NO_y$] ppb | [$O_3$] ppb | T (°C) | Concentration (μg/m3) | Average Size (nm) |
|---|---|---|---|---|---|---|---|---|
| Isoprene-LNOx | 1.0 | $H_2O_2$ | <1 | 5 | 3 | 25 | 40.8 | 326 |
| Isoprene-HNOx | 1.1 | $H_2O_2$ | 430 | 530 | 4 | 24 | 192 | 174 |
| Limonene[b] | 0.30 | Ozone | <1 | 6 | 590 | 24 | 1251 | 177 |

[a]The [HC] are the initial mixing ratios after injection of the liquid precursor, the remaining values were measured at the start of the sample collection.

[b]The Limonene chamber experiment was done in the dark.

**Table S5.** Average organic to inorganic thickness ratios for each campaign.

| Campaign | $d_{org}/d_{in}$ (% of thickness that is inorganic) | | |
|---|---|---|---|
| | In = S, metals etc | In=NaCl | In=$(NH_4)_2SO_4$ |
| CARES | 6.7 (13%) | 5.5 (15%) | 2.2 (31%) |
| MILAGRO | 7.8 (11%) | 6.4 (13%) | 2.6 (28%) |
| NAOPEX | 7.2 (12%) | 5.9 (14%) | 2.4 (30%) |
| VOCALS | 3.6 (22%) | 2.9 (26%) | 1.1 (47%) |
| YACS | 7.7 (12%) | 6.3 (14%) | 2.5 (28%) |